Energy & Environmental Science

Cite this: *Energy Environ. Sci.*, 2011, **4**, 2249

www.rsc.org/ees

PAPER

Enhancement of $La_{0.6}Sr_{0.4}Co_{0.2}Fe_{0.8}O_{3-\delta}$ durability and surface electrocatalytic activity by $La_{0.85}Sr_{0.15}MnO_{3\pm\delta}$ investigated using a new test electrode platform†

Matthew E. Lynch,‡ Lei Yang,‡ Wentao Qin,‡ Jong-Jin Choi,§ Mingfei Liu, Kevin Blinn and Meilin Liu*

Received 17th February 2011, Accepted 23rd March 2011
DOI: 10.1039/c1ee01188j

A carefully designed test cell platform with a new electrode structure is utilized to determine the intrinsic surface catalytic properties of an electrode. With this design, the electrocatalytic activity and stability of an $La_{0.6}Sr_{0.4}Co_{0.2}Fe_{0.8}O_{3-\delta}$ (LSCF) cathode is enhanced by a dense thin $La_{0.85}Sr_{0.15}MnO_{3\pm\delta}$ (LSM) coating, suggesting that an efficient electrode architecture has been demonstrated that can make effective use of desirable properties of two different materials: fast ionic and electronic transport in the backbone (LSCF) and facile surface kinetics on the thin-film coating (LSM). Theoretical analyses suggest that the enhanced electrocatalytic activity of LSM-coated LSCF is attributed possibly to surface activation under cathodic polarization due to the promotion of oxygen adsorption and/or dissociation by the surface layer and the dramatically increased oxygen vacancy population in the surface film. Further, the observed time-dependent activation over a few hundreds of hours and durability are likely associated with the formation of a favorable hybrid surface phase intermediate between LSM and LSCF. This efficient electrode architecture was successfully applied to the state-of-the-art LSCF-based cathodes by a simple solution infiltration process, achieving reduced interfacial resistance and improved stability under fuel cell operating conditions.

1 Introduction

Solid oxide fuel cells (SOFCs) represent the cleanest, most efficient and versatile chemical-to-electrical energy conversion system.[1,2] One of the grand challenges facing the development of a new generation of SOFCs is the creation of a cathode material with low overpotential at intermediate temperature.[3,4] The primary properties of a promising cathode are a) fast transport of ionic/electronic species, b) rapid surface electrochemical reactions, c) chemical interaction and thermal expansion compatible with other SOFC materials, and d) stability at high temperature in oxidizing atmosphere. Recent efforts at developing suitable cathodes for intermediate temperature SOFCs have focused on developing new materials with more favorable intrinsic oxygen reduction properties such as those in the $Ba_{1-x}Sr_xCo_{1-y}Fe_yO_{3-\delta}$ or double perovskite families,[5,6] creating more efficient electrode architectures through infiltration of active material,[7] and surface modification through infiltrated catalyst decoration.[8–10]

School of Materials Science and Engineering, Georgia Institute of Technology, 771 Ferst Dr, NW, Atlanta, GA 30332-0245, USA. E-mail: meilin.liu@mse.gatech.edu

† Electronic supplementary information (ESI) available. See DOI: 10.1039/c1ee01188j

‡ These authors contributed equally to this work

§ Current address: Functional Ceramics Group, Korea Institute of Materials Science, 797 Changwondaero, Sungsan-gu, Changwon, Gyeongnam, 642-831, Korea

Broader context

Solid oxide fuel cells (SOFCs) offer an attractive combination of high efficiency, fuel flexibility, and distributed power generation and are an important component of environmentally conscious alternative energy technology. To enable widespread commercialization of SOFCs, however, the performance of the porous cathode has to be further enhanced, more so at lower operating temperatures. In this contribution, we report a new electrode architecture for performance enhancement: a porous backbone of high ionic and electronic conductivity, such as $La_{0.6}Sr_{0.4}Co_{0.2}Fe_{0.8}O_{3-\delta}$ (LSCF), coated with a thin-film coating of a catalyst having high stability and catalytic activity toward O_2 reduction, such as $La_{0.85}Sr_{0.15}MnO_{3\pm\delta}$ (LSM). The concept feasibility has been demonstrated by both experimental measurements and theoretical analyses of LSM-coated LSCF cathodes. However, the electrode architecture is applicable to other materials combinations for SOFC or other electrochemical applications.

Currently, no single cathode material or approach can meet all of the requirements for intermediate temperature SOFCs.

$La_{0.85}Sr_{0.15}MnO_{3\pm\delta}$ (LSM) and $La_{0.6}Sr_{0.4}Co_{0.2}Fe_{0.8}O_{3-\delta}$ (LSCF) cathodes are commonly used in SOFCs. It has been previously shown that LSM cathodes exhibit much lower ionic conductivity and more sluggish oxygen surface exchange kinetics than LSCF[11] due to a relative dearth of surface oxygen vacancies. LSCF has high ionic and electronic conductivity, potentially extending the active sites beyond the triple phase boundary (TPB) to the surface of the LSCF far from the electrolyte.[12,13] However, the electrochemical activity of the stand-alone LSCF cathode is likely to be limited by the surface catalytic properties.[14,15] The dominant oxygen reduction reaction is associated with the surface exchange process.[16] Inadequate long-term stability of LSCF is also a primary factor impeding the widely practical commercial application.[17,18]

A few literature reports combine LSM and with other perovskites. LSM/YSZ functional layers have been used in conjunction with LSCF current-collector layers without intermixing of the perovskite phases.[19] Some success was achieved when hybrid phases of LSM and strontium-doped $LaCoO_3$ (LSC) were formed, denoted LSMC, or when the two phases were infiltrated sequentially onto a YSZ scaffold.[20]

In this study, we propose a new electrode architecture, consisting of a cathode backbone coated with a dense, thin-film catalyst in order to make effective use of the desirable properties of two different materials: the high ionic and electronic conductivity of an LSCF backbone and the excellent stability and high catalytic activity of an LSM coating. We examined this new electrode architecture by coating LSM as a thin layer onto LSCF, first by using a model electrode test cell platform with well-controlled geometry (see Fig. 1a for schematic illustration) to isolate the surface effects, then by a solution infiltration process to introduce a thin-film LSM coating onto the porous LSCF cathode. We found that a thin LSM coating does increase the performance under cathodic polarization and increases the durability as well.

This study presents an investigation of the LSM-coated LSCF architecture by several methods. The new model electrode test platform is used for fundamental evaluation of uncoated and LSM-coated LSCF cathodes. Full-cell testing is employed to examine durability and electrochemical performance of the coated and uncoated cathodes under practical fuel cell conditions. Transmission electron microscopy is used to examine compositional and structural properties of the LSM surface layer. Finally, theoretical reaction rate models are developed to relate electrochemically driven changes in point defect concentrations as well as time-dependent surface structure/composition changes to the observed electrochemical properties.

2 Experimental

2.1 Model electrodes

The purpose of the model electrode test cell platform is to create a well-defined geometry that allows the isolation of surface reactions. A discussion for the rationale of this test cell design is included in the Electronic Supplementary Information, section

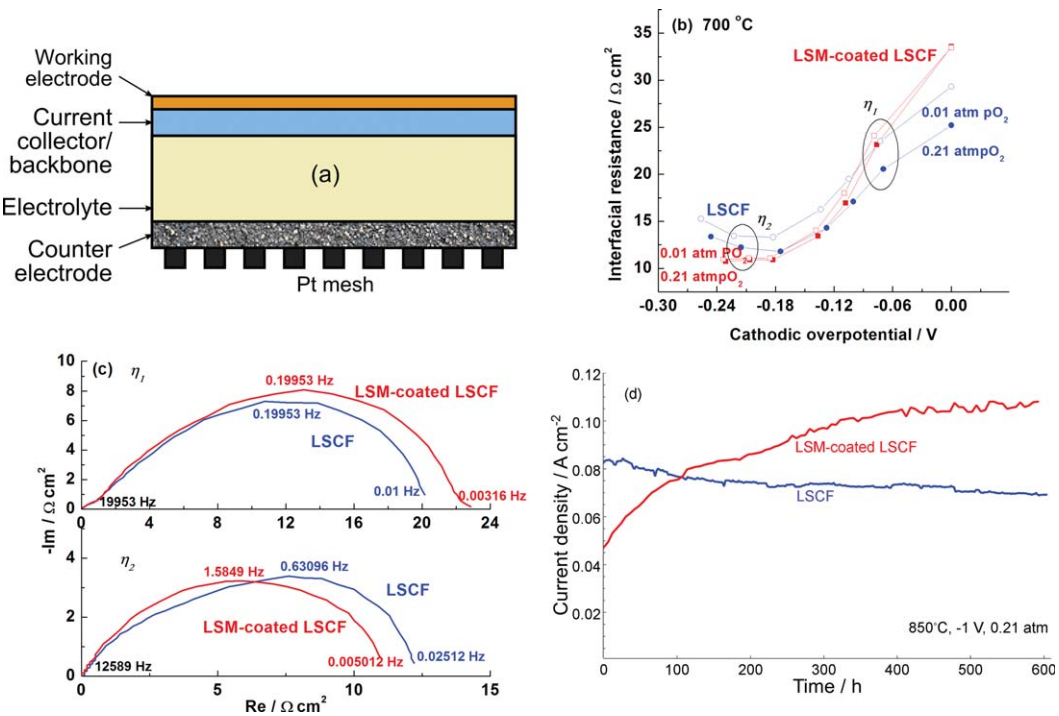

Fig. 1 a) Schematic diagram of the two-layer model electrode. b) Effect of cathodic overpotential on the interfacial resistances of blank LSCF and LSM-coated LSCF model electrodes under different oxygen pressures. c) Impedance spectra of blank LSCF and LSM-coated LSCF cathode without Ohmic portion at 700 °C under indicated cathodic overpotential conditions η_1 and η_2. d) Current densities of two model electrode cells with and without LSM coating as a function of time at a constant voltage of −1 V.

ESI 1. Gadolinium-doped ceria (GDC) powder with composition $Ce_{0.9}Gd_{0.1}O_{1.95}$ was pressed and sintered at 1450 °C into dense pellets and mechanically polished on both sides. The backbone and surface modification layers were deposited on the top by DC sputtering[16] (working pressure: 2.5×10^{-2} mbar, sputtering temperature: 300 °C) with thicknesses of 1 μm and 10 nm, respectively. A highly active, porous LSCF electrode was used as the counter electrode (CE) on the reverse side of the electrolyte and a Pt mesh was used as current collector to minimize the impedance of the CE.

The model electrodes were characterized by electrochemical impedance spectroscopy in flowing oxygen with different partial pressures (balanced by N_2) and at various cathodic biases. The test cells were so designed that the relaxation processes present in electrochemical impedance spectra were dominated by the processes relevant to electrochemical reactions on the surface of the model electrode and therefore a reference electrode was omitted. The model electrodes were also tested at a constant cell voltage of −1 V while the current densities were measured as a function of time. All standard electrochemical experiments were conducted using a Solartron 1286 electrochemical interface and a Solartron 1255 HF frequency response analyzer.

Raman spectroscopy of the model electrodes was performed using a Renishaw 1000 Raman Spectromicroscope (514 nm, 25 mW).

2.2 Full cells

Anode-supported fuel cells for performance and stability testing were fabricated with configuration consisting of Ni-YSZ composite anode (800 μm)/YSZ electrolyte (15 μm)/SDC buffer layer (~3 μm)/LSCF cathode (50 μm). The cells were measured with humidified hydrogen (3 vol% H_2O) as fuel and stationary air as oxidant. Solution infiltration of cathodes was performed prior to testing.

A solution infiltration technique has recently been introduced in SOFC electrodes and shows great promise in the development of nanostructured electrodes.[21,22] In this study, a similar process was utilized to deposit thin LSM coatings onto the LSCF.[23] To fabricate the coating in the porous LSCF cathode, appropriate amounts of $La(NO_3)_3$, $Sr(NO_3)_2$ and $Mn(NO_3)_2$ were dissolved in a mixture of water and ethanol (1 : 1, vol/vol) to prepare 0.03 mol L^{-1} LSM solution. Glycine was added as the chelating agent (the molar ratio of glycine to metal was ~1.3 : 1). Polyvinyl pyrrolidone (PVP) was used (~5 wt% relative to the amount of LSM) as surfactant to improve the wetting of the solution onto the LSCF backbone. 8 μl of LSM solution was infiltrated into porous LSCF electrode (superficial area of ~0.3 cm^2) using a microliter syringe in order to accurately control the amount of solution. After allowing the solution to soak into the porous cathode and dry in air for 30 min, the infiltrated cells were fired at 900 °C for 1 h to obtain the desired phase of LSM.

Transmission electron microscopy (TEM) samples of the infiltrated cathode were prepared with the method of Focused Ion Beam (FIB) *in situ* lift-out. A thin carbonaceous layer was first applied to protect the sample surface. The FIB was carried out with a Hitachi NB5000 FIB-SEM operated at 40 kV. A thin sliver about 1.5 μm thick, 15 μm wide and 2 μm deep below the surface was lifted and bonded to a copper grid, after which the sample was further thinned to electron transparency. Subsequently the finished sample was examined in an HF3300 TEM/STEM/EDS equipped with a field emission gun and operated at 300 kV.

2.3 Solution-coated dense LSCF

To further assess film characteristics, films were deposited onto dense LSCF pellets by spin coating using a non-aqueous sol. The LSM sol with a concentration of 0.30 mol L^{-1} was prepared by dissolving proper amounts of $La(NO_3)_3 \cdot 6H_2O$, $Sr(CH_3COO)_2$, and $Mn(CH_3COO)_2 \cdot 4H_2O$ (all 99.9%, Aldrich Chemical Co., Milwaukee, WI) in mixed solvents at room temperature (~25 °C). A mixture of 2-methoxyethanol and acetic acid (all 99.9%, Aldrich Chemical Co., Milwaukee, WI) was used as the solvent. The volume fraction of acetic acid in the solvent was varied from 0 to 2/3 to optimize the stability and wettability of the sol and the best value was found to be 1/3. The prepared sol was aged for 1 day before thin film deposition. The deposited films were pyrolyzed at 300 °C for 10 min. on a digitally controlled hot-plate and then annealed at 900 °C for 1 h in an electric furnace with a heating rate of 3 °C/min. Dense LSCF pellets were uniaxially pressed from powders, sintered, and mechanically polished.

TEM analysis was conducted with similar procedure as on the porous cathode. STEM and EDS were conducted with an electron probe with a size of about 5 Å. Material compositions were determined based on standardless quantification in the thin-film approximation and with O excluded due to the strong absorption of O Kα X-ray. The atomic percents at any probed position were normalized to 40% to be consistent with the nominal sum of 40% of the A site and B site cations.

3 Results and discussion

3.1 Model electrode testing

Based on this new cell design, electrochemical performance of blank (that is, LSCF model electrodes with no LSM coating) and LSM-coated LSCF model electrodes were characterized under cathodic polarization. Fig. 1b shows the trend of interfacial resistance with cathodic bias. Without any bias (at OCV) and at small cathodic overpotentials, the blank LSCF shows lower interfacial resistance than the LSM-coated LSCF. This can be explained by the larger surface exchange coefficient of LSCF at near-equilibrium conditions.[24] However, by further applying DC bias, LSM-coated LSCF undergoes a rapid drop of interfacial resistance while a slower decrease was observed for the blank LSCF. The disparity is ascribed primarily to the difference in polarization behavior between LSM and LSCF. It has been reported in the literature that the interfacial resistance of LSM cathode can be reduced remarkably[25] while much smaller reduction of resistance is observed for LSCF upon initial application of cathodic current.[26] Interestingly, an increase in interfacial resistance was observed for the blank LSCF electrode upon further bias (when $\eta < \eta_2$), thereby causing a more obvious difference.

Fig. 1c gives representative interfacial impedance spectra for blank and LSM-coated LSCF model electrodes in air under the two cathodic polarizations ($\eta_1 \sim -0.08$ V and $\eta_2 \sim -0.2$ V)

indicated in Fig. 1b. These two spectra share similar features in which the impedance shrinks in the low-frequency range when going to more cathodic bias. It is generally reported that the low-frequency arc for a dense LSCF cathode is assigned to surface exchange reactions.[27] These results indicate that thin LSM coating may enhance surface activity.

When blank and LSM-coated LSCF electrodes were exposed to 1% O_2, the interfacial resistances of the blank LSCF electrode were increased. This behavior coincides with a result reported elsewhere,[28] suggesting that a rate-limiting step is associated with the surface adsorption/dissociation reaction on the LSCF surface. In contrast, LSM-coated LSCF exhibits much less dependence on oxygen pressure, resulting in the crossover point shifting to lower overpotentials compared with that in air.

The electrochemical stability of the model electrodes was examined under potentiostatic test conditions. Fig. 1d indicates the current density of test cells with LSCF and LSM-coated LSCF cathodes as a function of time in air under a cell voltage of −1.0 V at 850 °C. The LSM-coated LSCF model electrode experienced a gradual increase of the current in the studied range, which is similar to the conditioning behavior of the traditional LSM cathode. In contrast, a continuous degradation was observed for LSCF cathode. Simner[18] also observed the quick decrease of LSCF cathode performance during fuel cell operation.

3.2 Operational full-cell testing

Based on the positive result of the model electrode measurements, a simple solution infiltration process was used to fabricate an operational LSM-coated LSCF cathode. The goal of solution infiltration was to create a microstructure as shown schematically in Fig. 2a, with a uniform and dense coating of LSM covering the LSCF particles that comprise the porous cathode. A state-of-the-art anode-supported fuel cell with porous LSCF cathode was employed to investigate the performance and stability upon introduction of LSM thin coating.

The electrochemical performance was consistent with the model electrode experiments. Representative full interfacial impedance spectra of blank and LSM-coated porous cathodes are given in Fig. 2b. The interfacial resistance of the LSM-coated cathode is larger at OCV but smaller under cathodic bias. Fig. 2c displays the current density change of the blank cell and the LSM-infiltrated cell with time under constant voltage of 0.7V at 750 °C. The performance of the LSM-coated LSCF cathode-containing cell initially had lower performance because the starting cathodic overpotential was approximately −0.1 V, which is closer to OCV than the crossover point leading to superior performance of the infiltrated cell (*cf.* model electrode data, Fig. 1b). However, the cell displayed a time-dependent activation that led to a considerable increase in performance in the first 200 h of operation. This increase contrasts with the rapid decrease in performance of the blank LSCF cell in the same time period. Considering the extremely stable anode of the commercial cells, the degradation behavior is associated with cathode phenomena. These behaviors are consistent with the behaviors of LSM-coated LSCF model electrodes (Fig. 1d). Fig. 2d gives the dependence of cell voltages and power densities on current density at 700 °C for fuel cells using LSCF and LSM-coated LSCF cathodes after long-term operation. An obvious

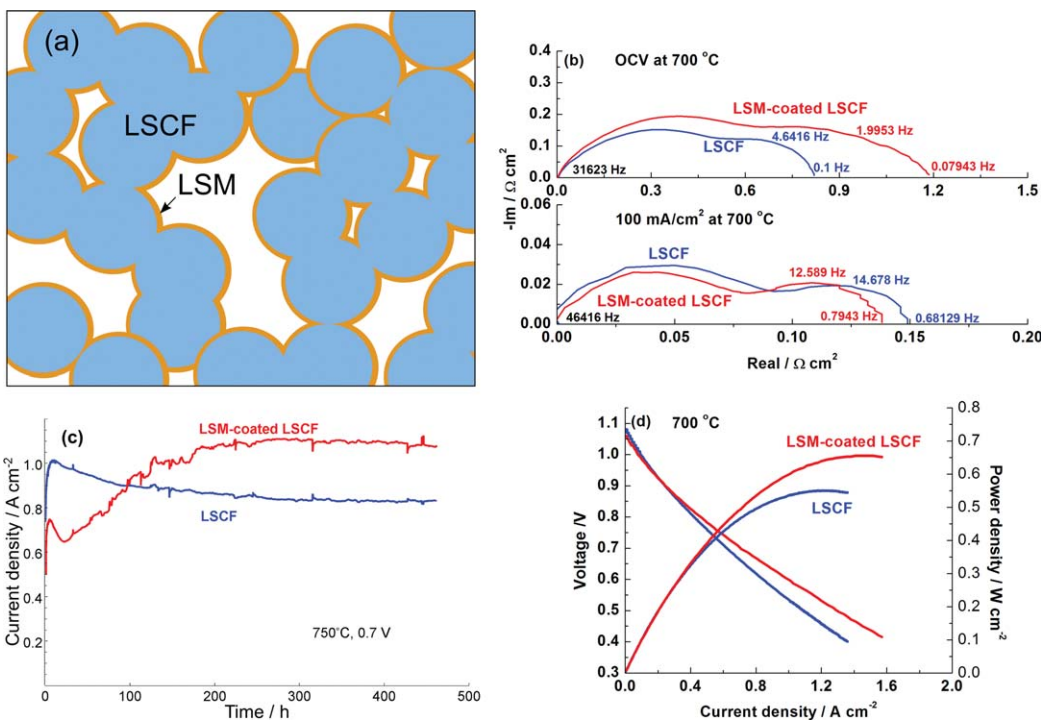

Fig. 2 a) Schematic diagram of the LSM-infiltrated LSCF cathode. b) Impedance spectra of fuel cells with and without infiltration of LSM measured at OCV and at 100 mA cm^{-2}, without Ohmic portion. c) Current density of two test cells with and without infiltration as a function of time under a constant voltage of 0.7 V and approximate cathodic overpotential of −0.12 V. d) Cell voltages and power densities as a function of current density for full cells with and without infiltration of LSM after long term testing.

discrepancy in peak power densities was observed for the LSM-infiltrated cell and blank cell, that is, 655 and 549 mW cm^{-2}, respectively. The peak power density of LSM-infiltrated cell appears to be superior to reports of LSMC hybrid-phase performance a sequentially infiltrated LSM-LSC composites,[20] which had peak power densities of 305 mW cm^{-2} and ~400–500 mW cm^{-2}, respectively, at 700 °C. The time-dependent activation displayed by the LSM-infiltrated LSCF cathode in this study further contrasts with the decrease in power density of the sequential LSM-LSC cathode in the first 250 h of operation.[20]

The LSM-infiltrated LSCF cathode was examined by TEM of a cell operated at 0.8 V for 900 h at 750 °C (Fig. 3). It can be seen from the view of a particle taken from the cathode in Fig. 3a that it is coated with a uniform, continuous, and dense surface film whose projected thickness varies between 2 and 23 nm, largely validating the schematic design in Fig. 2a. The continuity of the coating is attributed to the close structural similarity of LSM and LSCF, which causes a coherent coating to form more easily than in the case of other infiltrated materials that tend to form isolated particles.

A close view of the near-surface region in Fig. 3d shows the surface in clear contrast with the LSCF particle. After operation, the LSCF particle retains its perovskite structure, demonstrated by the zone-axis lattice fringes both deep in the bulk and near the surface of the LSCF grain, shown in Fig. 3b–e, while the outer portion of the infiltrated layer loses crystallinity, as demonstrated by the convergent beam electron diffraction (CBED) pattern in Fig. 3f.

Based upon the model electrode and full-cell data, it appears that there are two groups of enhancement mechanisms active in the LSM-coated LSCF cathode. The first is a purely electrochemical phenomenon due to enhanced electrocatalytic activity of the LSM surface under cathodic polarization. The second is a time-dependent activation originating from changes in structure, composition, and morphology of the LSM thin-film coating and the LSM/LSCF interface due to inter-diffusion over a longer period of time (a few hundreds of hours) during operation. The structural evolutions gradually result in superior performance and durability of the LSM-coated LSCF cathodes, even at overpotentials insufficient to cause superior performance through electrochemical activation.

3.3 Proposed electrochemical and structural mechanisms affecting the surface layer

Four possible mechanisms will be examined in detail. First, LSM may somehow favorably alter the surface, preventing degradation of performance with time. Second, the bulk pathway of the surface layer may be activated to a larger extent under a given cathodic polarization than is characteristic of bulk LSCF. Third, the presence of the Mn cation on the surface may promote adsorption/dissociation of oxygen relative to LSCF. Finally, structural defects in the film and space-charge effects may provide a fast ionic transport pathway in the surface layer relative to bulk LSM.

3.3.1 Surface stabilization and prevention of LSCF degradation. We used advanced electron microscopy and spectroscopy to examine the morphology, composition, and structure of the LSM and LSCF surfaces as well as the LSM/LSCF interface before and after long-term annealing. Fig. 4a shows the cross-sectional view (TEM image) of a sol–gel deposited surface layer in the as-deposited state on a dense LSCF pellet, while Fig. 4b shows the cross-sectional view of a similar surface layer after annealing at

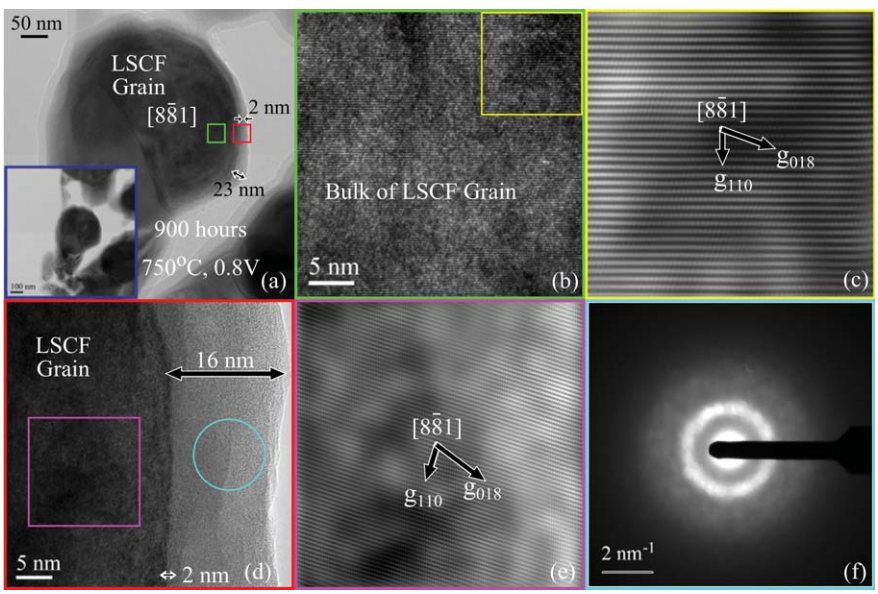

Fig. 3 TEM micrographs of an LSCF particle from an infiltrated porous electrode after long-term operation (750 °C, 0.8 V, 900 h). a) The whole particle, covered with an amorphous coating. b) zone-axis lattice image of the bulk of the particle in the green rectangle area in (a). c) Fourier-filtered image of the area within the yellow rectangle in (b). d) High-resolution view of the outer portion of LSCF grain and surface layer, highlited in the red rectangle in (a), and e) Fourier-filtered image of the area within the purple rectangle in (d). Zone-axis images in (c) and (e) indicate the LSCF grain retained perovskite structure after operation. f) CBED of the surface layer, indicating a loss of crystallinity.

850 °C for 900 h (under zero-current conditions). Fig. ESI1 gives additional TEM images of the interface prior to annealing. Fig. ESI2 gives additional TEM images after long-term annealing of a pellet. TEM images of the infiltrated porous cathode after operation have been presented in Figure ESI1. These images indicate that the sol–gel deposited layer is crystalline and is epitaxial with the underlying LSCF immediately after deposition and that that the portion of the surface film closest to the LSCF interface remains crystalline and epitaxial while the rest of the film loses long-range order and becomes amorphous after the long-term anneal.

Fig. 4c and d show EDS composition profiles of the surface layer and outermost portion of the underlying LSCF in the as-deposited state (c) and in the long-term annealed state (d). The surface layer retains Mn during long-term annealing but also experiences an addition of Co. There were no signs of strontium enrichment or surface phase segregation. Raman spectroscopy was also used to examine the stability (see section ESI 2 and Fig. ESI3). Peak shifts were observed on the blank LSCF after operation but no peak shifts were observed for the LSM-coated LSCF, indicating that the LSM-coated LSCF cathode has superior chemical stability.

Based upon the composition profiles, we suspect that during the course of high-temperature annealing and/or operation, Co diffuses from the underlying LSCF into the surface layer while Mn is mostly retained in the surface layer. Concurrently, the outer ~80% of the surface layer loses long-range order associated with crystallinity. The surface layer, then, is not truly LSM but rather becomes a hybrid with properties residing between those of LSM and LSCF due to the presence of introduced transition metal ions in the surface layer. We will denote this hybrid surface layer as LSM(C) owing to the majority concentration of Mn, while acknowledging the appreciable concentration of Co. A schematic diagram of the transformation from LSM to LSM(C) is shown in Fig. 4e.

3.3.2 Coating cathodic activation. There is evidence in the literature of an appreciable bulk pathway in thin LSM[29–32] activated especially under a large cathodic bias,[31,32] an effect attributed to a large addition of oxygen vacancies to the LSM under cathodic polarization. With the requirement that the LSM film be thin in order to mitigate bulk oxygen transport limitations, it is possible for the LSM coating to be strongly activated under cathodic bias due to large relative oxygen vacancy concentration increase.

We examined very simple surface kinetics to understand the cathodic activation phenomenon. Suppose that the current is proportional to the concentration of oxygen vacancies near the surface

$$i \propto \left(\frac{c_v}{c_v^0} - 1 \right) \quad (1)$$

This expression has a forward and backward term, with only the forward term being significantly affected by a change in the oxygen vacancy concentration. This treatment roughly represents the case where the rate-determining step is oxygen incorporation into the lattice or oxygen adsorption requiring mediation by an oxygen vacancy.[33,34] Treating the kinetics this way neglects the influence of other important species in the reaction; nevertheless it makes plain the role of oxygen vacancies in bulk activation and is useful for the present discussion. Such dependence allows rough comparison for the case where the limiting step for all overpotentials (not just near OCV) is dependent upon oxygen vacancy concentration.

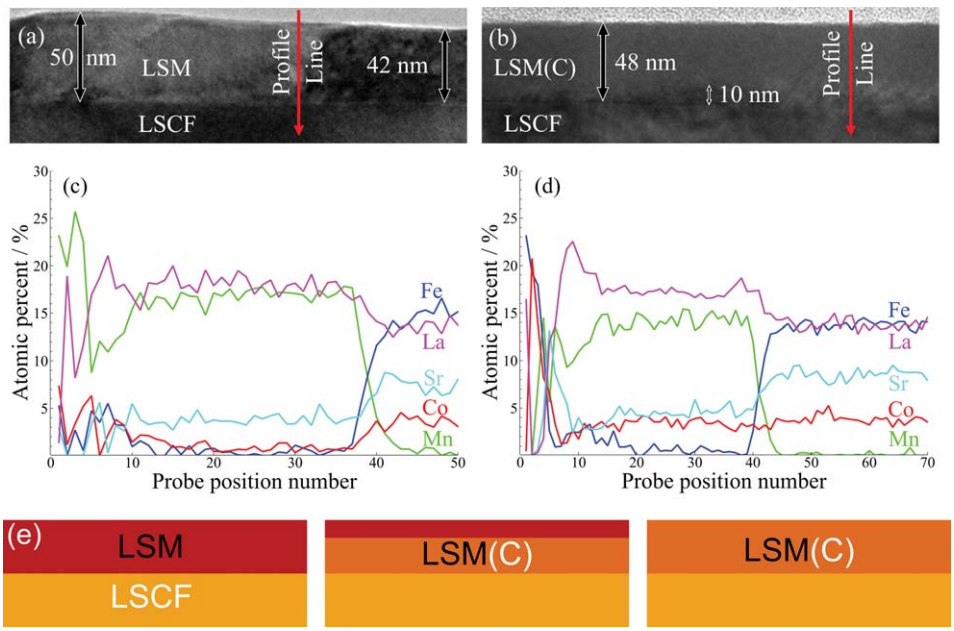

Fig. 4 Cross-sectional TEM micrograph of a sol–gel LSM-modified LSCF surface a) in the as-deposited condition and b) after long-term annealing at 850 °C for 900 h. EDS compositional profiles across the sol–gel surface layer and outermost part of LSCF layer c) in the as-deposited condition and d) after long-term annealing. e) Schematic illustration of role of in-diffusion to the LSM surface layer starting from the as-deposited LSM condition (left) and transforming into LSM(C) with high temperature annealing and/or operation.

The surface interfacial resistance, R_i, can be computed from the change of current, i, and overpotential, η, at steady state

$$R_i = \frac{\partial \eta}{\partial i} = -\frac{1}{4F}\frac{\partial \eta}{\partial r} \quad (2)$$

by calculating the rate of molecular oxygen reduction, r, at given values of η. R_i does not include the effects of ionic or electronic transport.

Consider the defect chemistry of bulk LSM *versus* LSCF[35–37] (see the Brouwer diagrams in Fig. ESI4). The use of the bulk defect chemistries serves as an instructive guide to the point defect trends that may occur in the surface phase. Oxygen vacancy concentration is quite high in LSCF, whereas it is very low in LSM.

The overpotential was related to the steady state point defect concentrations (*e.g.* oxygen vacancy concentration, c_v) *via* the effective internal oxygen partial pressure, p_{O2}^{internal}, associated with the overpotential. Bulk oxygen vacancy concentrations for a given η were determined by converting η to p_{O2}^{internal} *via* Equation S1 (the Nernst relationship) and then used in the rate equation. A full discussion of this modeling approach is included in section ESI 3.

Simulated R_i of LSM and LSCF were computed and are plotted in Fig. 5a. Each resistance is normalized to its value at OCV to provide a relative comparison of the trends. R_i of LSCF initially decreases with cathodic polarization but increases again because the rate of vacancy increase slows at more severe cathodic polarizations. R_i of LSM decreases monotonically as the overpotential becomes more negative because the rate of increase of oxygen vacancies does not slow. Therefore, a surface layer that is strongly activated under cathodic polarization has the potential to be very active toward oxygen reduction under cathodic bias and could provide the superior performance observed experimentally in the case of LSM modification. A hybrid LSM(CF) film that forms over the long term might be expected to have properties intermediate between LSM and LSCF owing to mixed effects of the transition metal cations. Such a film could be more activated under cathodic bias than pure LSCF. To study cathodic activation as a function of degree of oxygen binding, we computed the defect chemistry for LSCF[37] with different values of the standard free energy of oxygen reduction, ΔG_{red}^0. Changing the energy in this manner has two effects: lowering the equilibrium oxygen vacancy concentration and altering the trend of oxygen vacancies with pO_2, causing the material to display a larger degree of activation with bias and as a consequence become more like LSM. Oxygen vacancy concentrations associated with this changing parameter are plotted in Fig. ESI6. The interfacial resistances normalized to their OCV values are shown in Fig. 5b, again assuming current proportional to oxygen vacancy concentration (eqn (1)). As oxygen binding becomes stronger (ΔG_{red}^0 multiplied by a factor greater than one), R_i decreases more quickly as bias is applied. At large bias, the resistance is lower than that of LSCF and does not increase again until much more severe cathodic overpotentials.

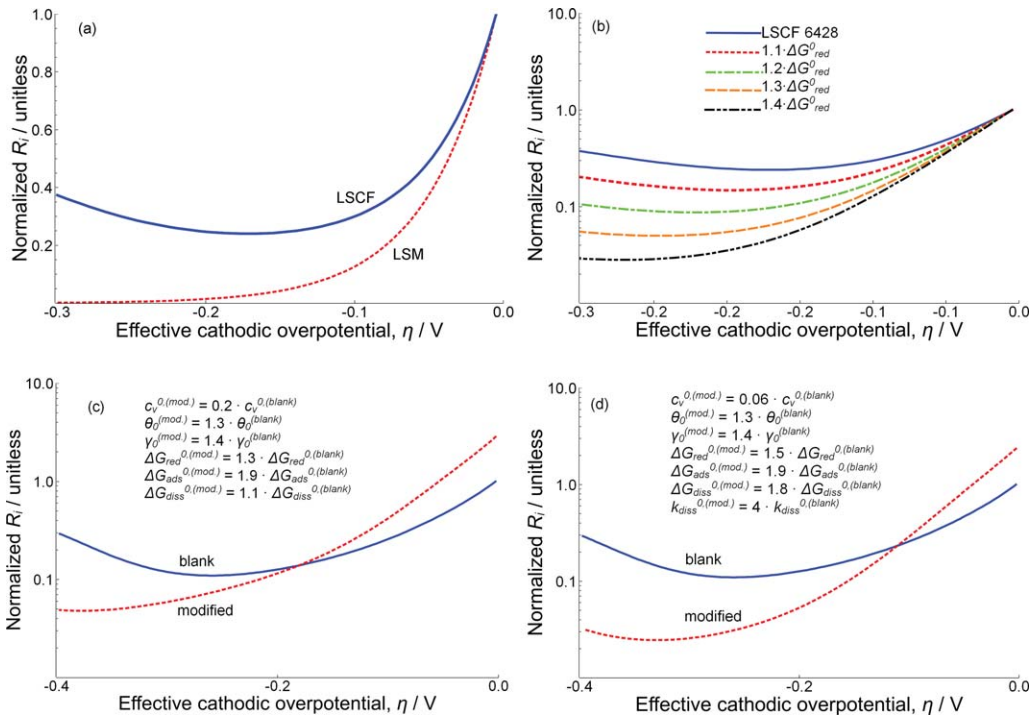

Fig. 5 a) Normalized interfacial resistance of LSCF and LSM films assuming that the current at the effective overpotential is described by eqn (1). Normalized to their respective values at OCV. b) Normalized interfacial resistance associated with tighter oxygen binding associated with lower free energy of oxygen reduction assuming current proportional to oxygen vacancy concentration. c) Simulated normalized interfacial resistance *versus* effective cathodic overpotential for blank LSCF and LSCF with modified surface properties when $\Delta G_{red}^{0(surface)} < \Delta G_{red}^{0(LSCF)}$, $\Delta G_{diss}^{0(surface)} < \Delta G_{diss}^{0(LSCF)}$, and $\Delta G_{ads}^{0(surface)} < \Delta G_{ads}^{0(LSCF)}$. R_i is normalized to the value of the blank LSCF at OCV. d) Simulated normalized interfacial resistance *versus* effective cathodic overpotential for blank and LSCF with modified surface properties when $\Delta G_{red}^{0(surface)} < \Delta G_{red}^{0(LSCF)}$, $\Delta G_{diss}^{0(surface)} < \Delta G_{diss}^{0(LSCF)}$, $\Delta G_{ads}^{0(surface)} < \Delta G_{ads}^{0(LSCF)}$, $k_{diss}^{0(surface)} > k_{diss}^{0(LSCF)}$.

This trend demonstrates that tighter oxygen binding can result in somewhat superior performance at large cathodic bias. A detailed discussion of this approach is included in section ESI 3.

3.3.3 Promoted adsorption/dissociation. More favorable adsorption and other surface steps such as oxygen dissociation lead to a large supply of oxygen available for incorporation and also lead to fast replenishment upon incorporation. Recently, DFT calculations[38] showed that adsorption energy is lower (more favorable) on LSM than on LSF and LSC due to the presence of the Mn cation, as opposed to the Co or Fe cations. Despite more strongly adsorbing oxygen, bulk LSM has a much smaller surface oxygen exchange coefficient than LSCF[39–41] most likely due to incorporation limitation associated with low oxygen vacancy concentration.

To give insight into the promoted adsorption/dissociation hypothesis, we modeled the process by classical, phenomenological chemical kinetics[42,43] and related the rate to the total interfacial resistance under cathodic steady state operation. Very little is known about the specific mechanisms of oxygen reduction on either LSM or LSCF surfaces. However, vacancy mediated adsorption/dissociation has been suggested for LSF[33,34] and LSM,[44] so we chose a variant for our analysis. For the sake of illustration, we assumed that the oxygen reduction process is characterized by the following reaction set

$$O_2(g) + * \leftrightarrow O_2^{2-}(s) + 2h^{\cdot} \quad (3)$$

$$O_2^{2-}(s) + V_o^{\cdot\cdot} \leftrightarrow O_o^{x} + O^{-}(s) + h^{\cdot} \quad (4)$$

$$O^{-}(s) + V_O^{\cdot\cdot} \leftrightarrow O_O^{x} + h^{\cdot} + * \quad (5)$$

where * represents a vacant surface site, $h^{\cdot}$ is an electron hole, $V_O^{\cdot\cdot}$ represents an oxygen vacancy and O_O^x represents a filled oxygen lattice site, both in Kröger-Vink notation. The three reactions represent the overall steps of adsorption, dissociation, and incorporation. This scheme[44] is in the general spirit of vacancy-mediated adsorption/dissociation.[33,34] Moreover, the O_2^{2-}(s) state has been suggested as a stable surface species.[44,45]

The reaction rates of these steps were written as follows:

$$r_{ads} = k_{ads,f} pO_2 (1-\gamma-\theta) \exp\left(-\frac{\alpha_a F}{RT}\chi_{ms}\right) - k_{ads,b}\gamma\, c_h^2 \exp\left(\frac{(2-\alpha_a)F}{RT}\chi_{ms}\right) \quad (6)$$

$$r_{diss} = k_{diss,f}\gamma\, c_v \exp\left(\frac{\alpha_d F}{RT}\chi_{ms}\right) - k_{diss,b}\theta\, c_O c_h \exp\left(-\frac{(1-\alpha_d)F}{RT}\chi_{ms}\right) \quad (7)$$

$$r_{inc} = k_{inc,f}\theta\, c_v \exp\left(\frac{\alpha_i F}{RT}\chi_{ms}\right) - k_{inc,b}(1-\gamma-\theta) c_O c_h \exp\left(-\frac{(1-\alpha_i)F}{RT}\chi_{ms}\right) \quad (8)$$

where γ is the fractional surface concentration [O_2^{2-}(s)], θ is the counterpart [O^-(s)], c_v is the oxygen vacancy concentration [$V_O^{\cdot\cdot}$], c_O is the concentration of filled oxygen sites [O_O^x] equal to c_{Osite}-c_v, c_h is the concentration of electron holes, and α_a, α_d, and α_i are transfer coefficients. The quantity χ_{ms} is the surface potential difference induced by dipoles associated with the charged adsorbates, equal to $\phi_m - \phi_s$ where $\phi_m$is the potential inside the MIEC and ϕ_s is the potential on the surface. Section ESI 4 outlines the derivation of these reaction rates.

The improvement of the LSM coating on blank LSCF was modeled by altering the surface parameters associated with blank LSCF. The overall energetics of the reactions were shifted from the values associated with uncoated LSCF in the direction indicated by theoretical studies for an LSM surface. That is, fewer oxygen vacancies and more favorable adsorption/dissociation compared to the blank LSCF. The point defect chemistry of modified LSCF (LSCF with more negative ΔG^0_{red}) developed in the previous section was used for this purpose. Section ESI 4 provides detail on this approach.

The result is shown in Fig. 5c and d. In Fig. 5c, R_i is slightly larger for the LSM-coated sample at OCV, but drops faster with increasing negative overpotential eventually decreasing below R_i of the uncoated LSCF 6428. The behavior simulated by the present model is qualitatively similar to that observed experimentally.

If the analysis is taken one step further and an additional *catalytic* effect is ascribed to the presence of Mn ions, then the barrier to reaction would be expected to shrink as well. The result appears in Fig. 5d where $k_{diss}{}^0$ has been increased (note that dissociation was assumed to be rate limiting on the blank LSCF surface - see section ESI 4). As a result, the oxygen vacancy concentration of the modified layer is nearly ten times smaller than for blank LSCF but the OCV resistance is only slightly larger. R_i drops and soon becomes more favorable as cathodic overpotential becomes more negative in this case due to both *more favorable* and *faster* adsorption/dissociation. Section ESI 4 provides detail on this approach as well.

3.3.4 Mediation by geometry and structural defects. The thickness of the surface layer is likely crucial to its role as a catalyst layer. If too thick, oxygen transport limitations could negate its favorable surface properties. The literature contains evidence for the thickness dependence of the LSM bulk pathway.[29,46,47] The surface films formed in this work were dense, and on the order of 2–23 nm (Fig. 3).

Dislocations, grain boundaries, and other structural defects in the surface layer may also be important. Oxygen tracer diffusivity along the grain boundary at temperatures near 700 °C has been shown to be approximately three orders of magnitude larger than tracer diffusivities in the bulk LSM crystal.[48] This effect arises because the activation energy for diffusion along the grain boundaries is lower than in the bulk, oxygen vacancies segregate to grain boundaries, or both. DFT calculations have shown oxygen vacancies to have lower formation energy on the surface than in bulk,[45] with possible applicability to internal boundaries and structural defects.

A space-charge layer in the LSM may also cause the oxygen vacancy concentration to depart substantially from its bulk value. When LSM is deposited onto the LSCF surface, it forms a diffusion couple with vacancies crossing the LSM-LSCF phase boundary. Since the LSM film is so thin, enrichment of oxygen

vacancies may persist to the surface where oxygen reduction is accelerated by the larger-than-bulk oxygen vacancy concentration.

3.4 Conclusions

An LSM-coated LSCF cathode demonstrated both improved durability and performance based on electrochemical characterization in sputtered model electrodes and porous cells. The model electrode platform revealed the surface of LSM-coated LSCF is highly active towards the oxygen reduction reaction under a cathodic bias. The same trend in commercial cells authenticates the concept feasibility of this new electrode test cell design as well as the enhancement caused by LSM coating. The LSM-coated electrode demonstrated short-term electrochemical activation under an applied cathodic bias as well as a time-dependent activation due to the evolution of structure, composition, and morphology of the surface and interfaces. The time-dependent activation improved the performance of the LSM-coated LSCF cathode sufficiently to surpass that of the blank LSCF cathode, even when the operating overpotential was relatively low. Possible theoretical explanations attribute this increase in performance to the formation of a hybrid LSM(C) phase on the surface, superior adsorption of oxygen associated with a Mn cation, large relative increase of oxygen vacancies in the surface phase compared to that of LSCF under cathodic polarization, and structural defects in the surface film with beneficial results on oxygen reduction. A more detailed theoretical explanation, including further micro-kinetic modeling and detailed study of the surface phase defect chemistry, should be developed to fully explain the behavior of blank and LSM-coated LSCF at short times as well as after operation. A longer operation period (thousands of hours) of LSM-coated LSCF cathodes will also be needed to further validate the findings. Other potential coating materials and different compositions of LSCF will be investigated, with the aim of further optimizing the new electrode architecture and looking for more significant performance improvement.

Finally, in analyzing the potential benefits of this new electrode architecture, it is important to understand the impact on cell cost. Since only infiltration of a non-precious-metal oxide catalyst and post treatment are needed to apply it to current commercial cells, the additional manufacturing operation and materials content require merely a small cost increase. Moreover, considering the improvement in performance and stability achieved by this technology, a net decrease in cell cost could be reasonably expected. Therefore, the LSM-coated LSCF cathode may aid realization of widespread implementation of intermediate-temperature SOFCs.

Acknowledgements

This work was supported by the U.S. Department of Energy (DOE) SECA Core Technology Program under Grant No. DE-NT-0006557 and by the HetroFoaM Center, an Energy Frontier Research Center funded by the U.S. DOE, Office of Science, Office of Basic Energy Sciences (BES) under Award Number DE-SC0001061. The authors thank Jae-Wung Lee for preparation of the sputtered electrode films and acknowledge the use of Oak Ridge National Laboratory's SHaRE User Facility, sponsored by the Division of Scientific User Facilities, BES, U.S. DOE.

References

1 L. Yang, S. Z. Wang, K. Blinn, M. F. Liu, Z. Liu, Z. Cheng and M. L. Liu, *Science*, 2009, **326**, 126–129.
2 B. C. H. Steele and A. Heinzel, *Nature*, 2001, **414**, 345–352.
3 Z. P. Shao and S. M. Haile, *Nature*, 2004, **431**, 170–173.
4 L. Yang, C. Zuo, S. Wang, Z. Cheng and M. Liu, *Adv. Mater.*, 2008, **20**, 3280–3283.
5 W. Zhou, R. Ran and Z. P. Shao, *J. Power Sources*, 2009, **192**, 231–246.
6 W. Zhou, J. Sunarso, Z.-G. Chen, L. Ge, J. Motuzas, J. Zou, G. Wang, A. Julbe and Z. Zhu, *Energy Environ. Sci.*, 2011, **4**, 872–875.
7 J. M. Vohs and R. J. Gorte, *Adv. Mater.*, 2009, **21**, 943–956.
8 S. P. Jiang and W. Wang, *J. Electrochem. Soc.*, 2005, **152**, A1398–A1408.
9 A. Thursfield and I. S. Metcalfe, *J. Membr. Sci.*, 2007, **288**, 175–187.
10 M. Watanabe, H. Uchida, M. Shibata, N. Mochizuki and K. Amikura, *J. Electrochem. Soc.*, 1994, **141**, 342–346.
11 E. P. Murray, T. Tsai and S. A. Barnett, *Solid State Ionics*, 1998, **110**, 235–243.
12 E. P. Murray, M. J. Sever and S. A. Barnett, *Solid State Ionics*, 2002, **148**, 27–34.
13 L. Yang, Z. Liu, S. Z. Wang, Y. M. Choi, C. D. Zuo and M. L. Liu, *Journal of Power Sources*, 195, pp. 471–474.
14 J. A. Lane, S. J. Benson, D. Waller and J. A. Kilner, *Solid State Ionics*, 1999, **121**, 201–208.
15 M. Prestat, J. F. Koenig and L. J. Gauckler, *J. Electroceram.*, 2007, **18**, 87–101.
16 J. W. Lee, Z. Liu, L. Yang, H. Abernathy, S. H. Choi, H. E. Kim and M. L. Liu, *J. Power Sources*, 2009, **190**, 307–310.
17 S. J. Benson, D. Waller and J. A. Kilner, *J. Electrochem. Soc.*, 1999, **146**, 1305–1309.
18 S. P. Simner, M. D. Anderson, M. H. Engelhard and J. W. Stevenson, *Electrochem. Solid-State Lett.*, 2006, **9**, A478–A481.
19 J. H. Kim, R. H. Song, K. S. Song, S. H. Hyun, D. R. Shin and H. Yokokawa, *J. Power Sources*, 2003, **122**, 138–143.
20 Y. Y. Huang, J. M. Vohs and R. J. Gorte, *J. Electrochem. Soc.*, 2006, **153**, A951–A955.
21 S. D. Park, J. M. Vohs and R. J. Gorte, *Nature*, 2000, **404**, 265–267.
22 T. Z. Sholklapper, H. Kurokawa, C. P. Jacobson, S. J. Visco and L. C. De Jonghe, *Nano Lett.*, 2007, **7**, 2136–2141.
23 J.-J. Choi, W. Qin and M. Liu, *J. Am. Ceram. Soc.*, 2011, accepted.
24 J. Maier, *Solid State Ionics*, 1998, **112**, 197–228.
25 Y. Jiang, S. Z. Wang, Y. H. Zhang, J. W. Yan and W. Z. Li, *J. Electrochem. Soc.*, 1998, **145**, 373–378.
26 A. Esquirol, N. P. Brandon, J. A. Kilner and M. Mogensen, *J. Electrochem. Soc.*, 2004, **151**, A1847–A1855.
27 F. S. Baumann, J. Fleig, H.-U. Habermeier and J. Maier, *Solid State Ionics*, 2006, **177**, 1071–1081.
28 A. Endo, H. Fukunaga, C. Wen and K. Yamada, *Solid State Ionics*, 2000, **135**, 353–358.
29 E. Koep, D. S. Mebane, R. Das, C. Compson and M. Liu, *Electrochem. Solid-State Lett.*, 2005, **8**, A592–A595.
30 G. J. la O', B. Yildiz, S. McEuen and Y. Shao-Horn, *J. Electrochem. Soc.*, 2007, **154**, B427–B438.
31 E. Siebert, A. Hammouche and M. Kleitz, *Electrochim. Acta*, 1995, **40**, 1741–1753.
32 V. Brichzin, J. Fleig, H.-U. Habermeier, G. Cristiani and J. Maier, *Solid State Ionics*, 2002, **152–153**, 499–507.
33 J. E. tenElshof, M. H. R. Lankhorst and H. J. M. Bouwmeester, *J. Electrochem. Soc.*, 1997, **144**, 1060–1067.
34 M. Mosleh, M. Sogaard and P. V. Hendriksen, *J. Electrochem. Soc.*, 2009, **156**, B441–B457.
35 F. W. Poulsen, *Solid State Ionics*, 2000, **129**, 145–162.
36 D. S. Mebane, Y. Liu and M. Liu, *Solid State Ionics*, 2008, **178**, 1950–1957.
37 S. R. Bishop, K. L. Duncan and E. D. Wachsman, *J. Electrochem. Soc.*, 2009, 156.
38 Y. Choi, M. C. Lin and M. Liu, *J. Power Sources*, 2010, **195**, 1441–1445.

39 R. A. De Souza and J. A. Kilner, *Solid State Ionics*, 1998, **106**, 175–187.
40 R. A. De Souza and J. A. Kilner, *Solid State Ionics*, 1999, **126**, 153–161.
41 S. J. Benson, R. J. Chater and J. A. Kilner, *Proc. - Electrochem. Soc.*, 1998, **97–24**, 596–609.
42 D. S. Mebane and M. Liu, *J. Solid State Electrochem.*, 2006, **10**, 575–580.
43 M. E. Lynch, D. S. Mebane, Y. Liu and M. Liu, *J. Electrochem. Soc.*, 2008, **155**, B635–B643.
44 Y. M. Choi, D. S. Mebane, M. C. Lin and M. Liu, *Chem. Mater.*, 2007, **19**, 1690–1699.
45 Y. L. Lee, J. Kleis, J. Rossmeisl and D. Morgan, *Phys. Rev. B: Condens. Matter Mater. Phys.*, 2009, **80**, 224101–224101.
46 J. Mizusaki, T. Saito and H. Tagawa, *J. Electrochem. Soc.*, 1996, **143**, 3065–3073.
47 A. Endo, M. Ihara, H. Komiyama and K. Yamada, *Solid State Ionics*, 1996, **86–88**, 1191–1195.
48 R. A. De Souza, J. A. Kilner and J. F. Walker, *Mater. Lett.*, 2000, **43**, 43–52.

